Ubiquitous velocity fluctuations throughout the molecular interstellar medium

Jonathan D. Henshaw [1 ✉], J. M. Diederik Kruijssen [2], Steven N. Longmore[3], Manuel Riener [1], Adam K. Leroy[4], Erik Rosolowsky[5], Adam Ginsburg [6], Cara Battersby[7], Mélanie Chevance [2], Sharon E. Meidt[8], Simon C. O. Glover[9], Annie Hughes[10,11], Jouni Kainulainen [12], Ralf S. Klessen [9], Eva Schinnerer[1], Andreas Schruba[13], Henrik Beuther[1], Frank Bigiel[14], Guillermo A. Blanc[15,16], Eric Emsellem [17,18], Thomas Henning[1], Cynthia N. Herrera [19], Eric W. Koch[5], Jérôme Pety[19,20], Sarah E. Ragan [21] and Jiayi Sun [4]

The density structure of the interstellar medium determines where stars form and release energy, momentum and heavy elements, driving galaxy evolution[1-4]. Density variations are seeded and amplified by gas motion, but the exact nature of this motion is unknown across spatial scales and galactic environments[5]. Although dense star-forming gas probably emerges from a combination of instabilities[6,7], convergent flows[8] and turbulence[9], establishing the precise origin is challenging because it requires gas motion to be quantified over many orders of magnitude in spatial scale. Here we measure[10-12] the motion of molecular gas in the Milky Way and in nearby galaxy NGC 4321, assembling observations that span a spatial dynamic range 10^{-1}–10^3 pc. We detect ubiquitous velocity fluctuations across all spatial scales and galactic environments. Statistical analysis of these fluctuations indicates how star-forming gas is assembled. We discover oscillatory gas flows with wavelengths ranging from 0.3–400 pc. These flows are coupled to regularly spaced density enhancements that probably form via gravitational instabilities[13,14]. We also identify stochastic and scale-free velocity and density fluctuations, consistent with the structure generated in turbulent flows[9]. Our results demonstrate that the structure of the interstellar medium cannot be considered in isolation. Instead, its formation and evolution are controlled by nested, interdependent flows of matter covering many orders of magnitude in spatial scale.

We use observations that trace molecular gas in a variety of galactic environments and span a wide range of spatial scales. We measure the position–position–velocity (p–p–v) structure of the molecular interstellar medium (ISM) from 0.1 pc scales, relevant for individual star-forming cores up to the scales of individual giant molecular clouds (GMCs), now accessible in nearby galaxies using facilities such as the Atacama Large Millimeter/submillimeter Array (ALMA). On large (from 100 pc to >1,000 pc) scales, we analyse observations of nearby galaxy NGC 4321 from the Physics at High Angular resolution in Nearby Galaxies (PHANGS-ALMA) survey. At intermediate (from 1 pc to 100 pc) scales, we target both the Galactic Disk and the Central Molecular Zone (CMZ, the central 500 pc) of the Milky Way with data from the Galactic Ring Survey[15] and the Mopra CMZ survey[16], respectively. On small scales (from 0.1 pc to around 10 pc), we include observations of two dense molecular clouds: G035.39–00.33 (ref. [17]) in the Galactic disk and G0.253+0.016 (ref. [11]) in the CMZ. We summarize the observations in Extended Data Fig. 1.

We extract the kinematics of the gas using spectral decomposition, modelling each spectrum as a set of individual Gaussian emission features[10-12]. Spectral decomposition is advantageous because it yields a description of all prominent emission features observed in spectroscopic data. We visualize the results using the peak intensities and velocity centroids of the modelled emission features (Fig. 1). This method facilitates the detection of small fluctuations in velocity, which can often be hidden by techniques that either average in the spectral domain or integrate over one of the two spatial directions. We discover striking similarity in the p–p–v structure of the molecular ISM in all of our selected environments, despite our observations probing vastly different spatial scales. The p–p–v volumes presented in Fig. 1 (see also Supplementary Videos 1–10) reveal the complex multiscale dynamical structure of the molecular ISM. The 'wiggles' evident in all datasets represent localized gas flows superposed on larger-scale ordered motion.

Measuring the dynamical coupling between ISM density enhancements and their local environment is key to understanding
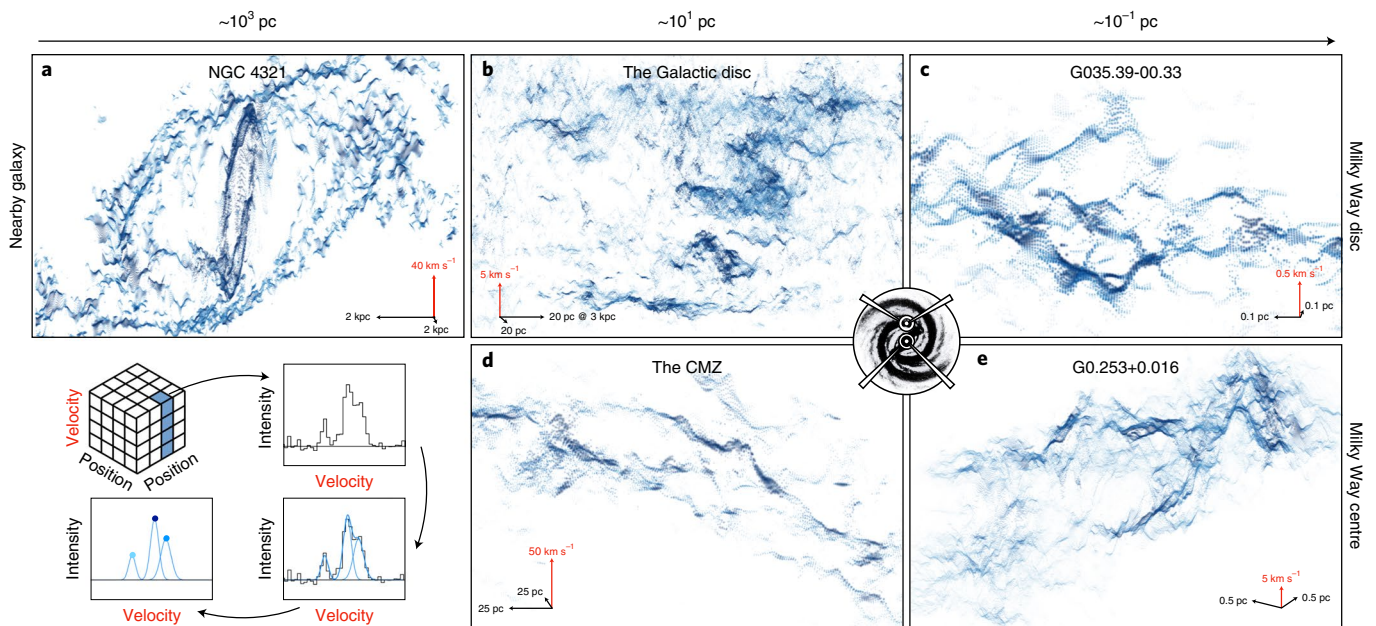
Fig. 1 | Ubiquitous velocity fluctuations throughout the molecular ISM. Here we show $p-p-v$ volumes of different galactic environments (see also Supplementary Videos 1–5). The data points indicate the $x-y$ positions and velocities of individual Gaussian emission features extracted from each dataset using spectral decomposition (see Methods). The colour indicates the peak intensity of each emission feature (see the cartoon in the bottom left). The different columns illustrate decreasing spatial scale, from kiloparsec scales on the left down to subparsec scales on the right. The rows highlight differences in galactic environments, from galaxy disks (top) to the CMZ (bottom). **a**–**e**, The individual regions are: NGC 4321 (**a**); a region in the Milky Way's Galactic Disk (**b**); the Northern part of the infrared dark cloud (IRDC), G035.39–00.33 (**c**); the inner 250 pc of the Milky Way (the CMZ) (**d**); and IRDC G0.253+0.016 (**e**). We include 3D scale bars in the bottom corners of each panel to indicate the physical scaling as well as the orientation of each $p-p-v$ volume. Note that our selected region in the Galactic Disk (**b**) contains gas located at different distances. The scale bar is correct for a distance of 3 kpc, which is relevant for the statistical analysis of our selected GMC (see Methods). Inset image credit: NASA/JPL-Caltech/R. Hurt (SSC-Caltech).

the formation of hierarchically structured star-forming gas[1]. The structure of dense gas that is weakly dynamically coupled to the local environment should show little or no correlation with observed gas flows. In contrast, density structures produced by ongoing convergent flows should be closely coupled to the gas flows[8,18]. In the specific case of instability-driven structure formation, preferred characteristic scales may be present in both density[6,19] and velocity. Between the scales of energy injection and dissipation, turbulence is instead characterized by scale-free fluctuations in both density and velocity[9].

We select a subregion from each dataset presented in Fig. 1 to represent the hierarchy of the ISM. We first select part of the southernmost dominant spiral arm in NGC 4321 and, in the CMZ, a portion of the gas orbiting the centre of the Galaxy at a galactocentric radius of about 100 pc. We then select two GMCs, one in the Galactic Disk and another in the CMZ. Finally, we select an individual filament that is embedded within our selected GMC in the Galactic Disk. Maps of all of the regions can be found in Extended Data Fig. 2.

We use structure functions to measure the coupling between the observed gas flows and the physical structure of the gas in each subregion (see Methods and Supplementary Information). Normalized, noise-corrected structure functions of velocity and gas density are presented in Fig. 2. The velocity structure functions measured in one dimension along the crests of the spiral arm of NGC 4321 (Fig. 2a) and in the CMZ gas stream (Fig. 2d) exhibit local minima at specific spatial scales. Structure functions display localized minima in response to periodicity in spatial or temporal data, indicating that the observed velocity fluctuations oscillate with an intrinsic wavelength (for an intuitive demonstration of this behaviour, see the Supplementary Information and Supplementary Fig. 1).

We measure the wavelengths of these oscillations as being 405^{+92}_{-76} pc and $22.0^{+5.4}_{-6.3}$ pc in the spiral arm and CMZ gas stream, respectively. The coherent nature of these oscillatory motions, detected over 10^2–10^3 pc scales, is inconsistent with the characteristically scale-free motion produced in a turbulent flow.

Inspection of the corresponding density structure functions reveals periodicity on equivalent spatial scales to that detected in velocity. In the spiral arm, we find a minimum located at 366^{+88}_{-77} pc. In the CMZ, two minima are identified at $6.0^{+0.8}_{-0.6}$ pc and $21.8^{+5.5}_{-6.3}$ pc, respectively. The periodicity implied by these localized minima corresponds to the regular spacing of molecular cloud complexes detected in CO (2–1) emission in the spiral arm of NGC 4321 and GMCs detected in dust continuum emission in the CMZ gas stream, respectively (emission profiles extracted along the crests of these structures are shown in Extended Data Fig. 3). The derived separation of the cloud complexes in the spiral arm of NGC 4321 agrees with the 410 pc spacing of embedded star clusters independently identified using mid-infrared observations[14]. Multiple minima detected in the density structure function of the CMZ gas stream suggest that GMCs separated by $6.0^{+0.8}_{-0.6}$ pc are clustered together in groups separated by $21.8^{+5.5}_{-6.3}$ pc. This is confirmed via inspection of the distribution of $N_2H^+(1-0)$ emission from which our velocity information is derived (see Supplementary Information).

The phase difference between the density and velocity fluctuations encodes the physical origins of the detected gas flows. In the spiral arm, we find that the velocities of the molecular cloud complexes are almost always blueshifted with respect to the rotational velocity of the galaxy at this location. The molecular cloud complexes, detected as peaks in the CO (2–1) emission, therefore reside where the velocity gradient is close to zero (Extended Data Fig. 4a). Combining knowledge of the inclination and rotation[14,20] of
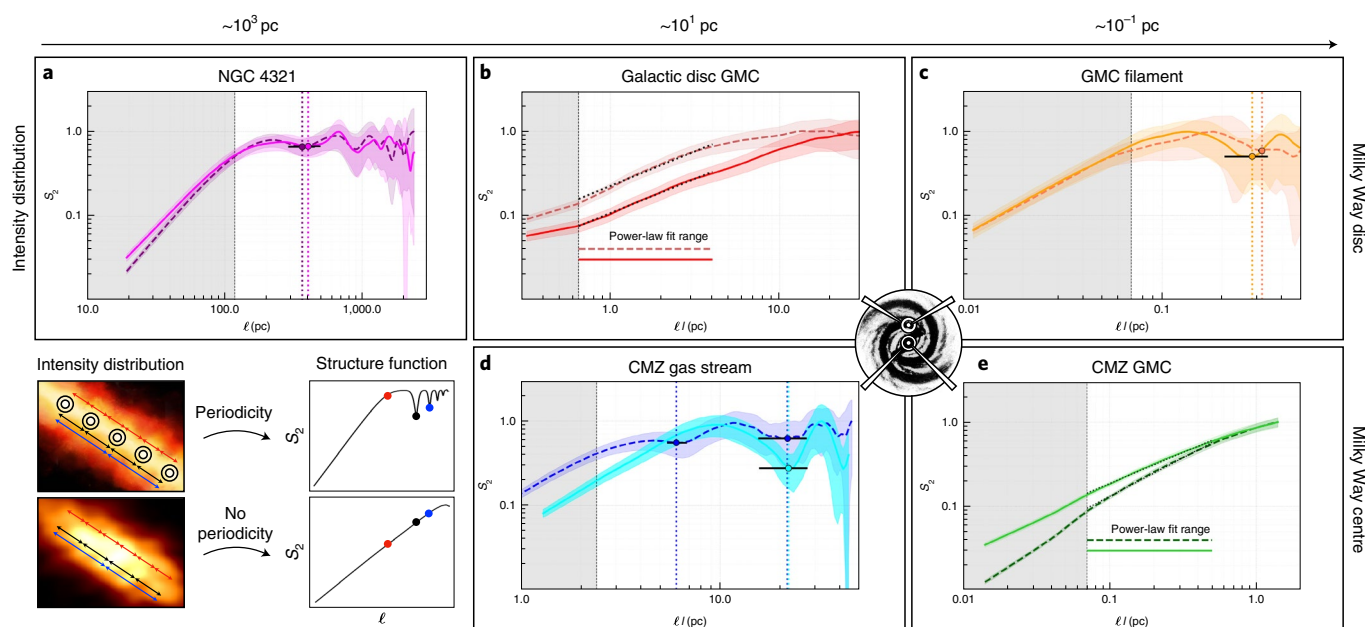
Fig. 2 | Correlated density and velocity fluctuations. Each panel shows normalized and noise-corrected second-order structure functions (S_2) of density (coloured dashed lines) and velocity (coloured solid lines) taken from a subsample of the datasets presented in Fig. 1. The regions selected for this analysis are shown in Extended Data Fig. 2 (see Methods). **a**, A portion of the southernmost dominant spiral arm in NGC 4321. **b**, A GMC located within the Galactic Disk. **c**, An individual filament located within the same GMC. **d**, A portion of the CMZ gas stream. **e**, A GMC located within the CMZ. Vertical coloured dotted lines in **a**, **c** and **d** indicate the spatial scale of periodic fluctuations in density and velocity (the horizontal black lines indicate the uncertainty on these measurements; Table 1). Black dotted lines in **b** and **e** are power-law fits to the structure functions (the fit range is indicated by the coloured horizontal dashed and solid lines). The dark grey shaded area indicates the range of lags for which the recovered structure function is unreliable owing to the limited spatial resolution of the data. Inset image credit: NASA/JPL-Caltech/R. Hurt (SSC-Caltech).

Table 1 | Characteristic length scales

Environment	Filament diameter (pc)	Density periodicity (pc)	Velocity periodicity (pc)
Spiral arm	122 ± 5	366^{+88}_{-77}	405^{+92}_{-76}
CMZ gas stream	—	$6.0^{+0.8}_{-0.6}$	—
	4.2 ± 0.2	$21.8^{+5.5}_{-6.3}$	$22.0^{+5.4}_{-6.3}$
GMC filament	0.107 ± 0.001	$0.32^{+0.01}_{-0.01}$	$0.28^{+0.06}_{-0.08}$

The beam-deconvolved diameters of the filamentary structures that exhibit periodicity, as well as the separation between periodically spaced density enhancements and the wavelength of the velocity oscillations determined from our structure function analysis presented in Fig. 2, are included. The two rows for the CMZ gas stream correspond to the two minima identified in the density structure function. Note that the density and velocity fluctuations observed throughout the GMCs selected in our study have no discernible characteristic scaling and are therefore not included in Table 1.

NGC 4321 with the location of our selected arm with respect to the corotation radius of the spiral pattern (7.1–9.1 kpc; ref. [21]), we conclude that the observed oscillation probably results from a combination of spiral streaming motions and radial gravitational inflow[22]. Conversely, in the CMZ, the locations of N_2H^+ (1–0) emission peaks spatially correlate with extrema in the velocity gradient (see Extended Data Fig. 4). This signature implies that the gas flows are converging towards the emission peaks. In this context, the GMCs observed in the CMZ gas stream may be the result of hierarchical collapse[8], whereby large-scale cloud complexes fed by flows on $22.0^{+5.4}_{-6.3}$ pc scales have fragmented into a series of GMCs separated by $6.0^{+0.8}_{-0.6}$ pc. Further discussion on the nature of these flows can be found in the Supplementary Information.

As molecular clouds form at the stagnation points of convergent flows, the kinetic energy cascading from large to small scales

contributes to the supersonically turbulent motions that produce the complex and scale-free structure observed within GMCs[9,18]. Indeed, in contrast to the characteristic scaling observed in the density and velocity structure described above, the internal physical structure of our selected GMCs in the Galactic Disk and in the CMZ is multidimensional, complex and without regularity (see Extended Data Fig. 2b,e). This is confirmed in Fig. 2b,e, where we show that the structure functions of both density and velocity scale as power laws. This scale-free behaviour is also reflected in structure functions computed over discrete azimuthal angles, indicating that the velocity fluctuations do not exhibit a preferred orientation (see Methods).

There is broad agreement between the scaling of our velocity structure functions (0.41 ± 0.01 and 0.37 ± 0.01 for the GMCs in the disk and CMZ, respectively) and the distribution of measured scaling exponents for the Galactic linewidth–size relationship[23], which is often interpreted as evidence for the presence of supersonic turbulence in molecular clouds[24]. However, we caution that the scaling of velocity structure functions has been interpreted in many different ways and may be subject to observational biases (see Supplementary Information). Despite the similarity in the scaling exponents of the two regions, the velocity fluctuations in the CMZ are greater than those in the disk by a factors of 10–100 when measured on a fixed spatial scale, consistent with the elevated levels of turbulence present within the inner Galaxy[10,23].

Shocks generated by supersonic turbulence contribute to the formation of the filamentary structure that pervades molecular clouds[9,25]. High-resolution observations of one of the density enhancements detected in our Galactic Disk GMC reveal a complex internal network of dense, velocity-coherent filaments[17] (see Extended Data Fig. 2b,c). Embedded within each of these filaments is a population of density enhancements representing the formation sites of individual stars and stellar systems[17,26]. In analogy to the gas

flows observed on much larger scales along the spiral arm of NGC 4321 and in the CMZ gas stream, we find that the velocity fluctuations observed along the spine of our selected GMC filament exhibit periodicity on $0.28^{+0.06}_{-0.08}$ pc scales (Fig. 2c). The wavelength of these velocity oscillations is comparable to the separation of density enhancements along the filament ($0.32^{+0.01}_{-0.01}$ pc). Furthermore, the locations of some of these density enhancements spatially correlate with extrema in the velocity gradient (Extended Data Fig. 4c), indicative of either convergent motion or collapse-induced rotation[27].

A promising candidate driving the formation of periodic density fluctuations, and their correlated gas flows, is gravitational instabilities. We find that the separation of the periodic density enhancements observed in the spiral arm, CMZ gas stream and GMC filament are factors of $3-5$ times greater than the beam-deconvolved diameters of their parent structures (122 ± 5 pc, 4.2 ± 0.2 pc and 0.107 ± 0.001 pc, respectively; see Table 1). Periodic density enhancements arranged like beads on a string along their parent filaments have been observed in nearby galaxy disks[6,14], as well as in local molecular clouds[19,28], and frequently show separation-to-diameter ratios consistent with those measured in this study (see the Supplementary Information). This measured ratio is consistent with theoretical work describing the gravitational fragmentation of filaments, both on large[29] and small[30,31] scales. Our findings now extend this result by showing that the separation-to-diameter ratio in the velocity structure of the ISM matches that of the density enhancements.

The combined analysis of density structure and gas kinematics, as well as the spatial dynamic range covered in our study, represents a novel approach to understanding gas flows in the ISM and their relation to the emergence of physical structure. Our results indicate that the formation and evolution of dense star-forming gas across this sample of environments is controlled by nested, interdependent gas flows. The natural next steps are to apply this approach to an unbiased sample of regions, as well as to synthetic observations of numerical simulations, which together will provide critical insight into the role that the galactic environment plays in setting the scale and magnitude of the gas flows that seed star formation in galaxies.

Methods

Environment selection. Our observations cover a spatial dynamic range of about four orders of magnitude, from kiloparsec scales in the nearby galaxy NGC 4321 down to 0.1 pc scales in the Milky Way. In the following section we describe our environment selection.

NGC 4321. Located in the Virgo cluster, NGC 4321 (M100) is a barred grand-design spiral galaxy of class SAB(s)bc[32]. The galaxy is highly structured with two well-defined spiral arms with strong symmetry[33]. The galaxy has a stellar bar and a nuclear ring with a radius of about 1 kpc (ref. [34]). Strings of regularly spaced star-forming regions extend over kiloparsec distances within thin dust filaments throughout its disk[14,35].

The Galactic Disk. On intermediate scales in the Milky Way Disk, we include observations of the massive ($5 \times 10^5\,M_\odot$; ref. [36]) GMF 38.1–32.4b (ref. [36]). GMFs are a class of elongated giant molecular clouds[36–39]. Our selection of GMF 38.1–32.4b is based on its association with the IRDC G035.39–00.33, which provides the basis for the high-resolution component of our study of galaxy disks (see below). GMF 38.1–32.4b is almost orthogonal to the Galactic Plane and has a length of 80 pc and an aspect ratio about 1:12 (refs. [36,40]).

G035.39–00.33. Situated at a kinematic distance of 2.9 kpc (ref. [41]), G035.39–00.33 is a massive ($104\,M_\odot$; ref. [42]) and filamentary IRDC embedded within GMF 38.1–32.4b and is thought to harbour the early stages of star formation[43,44]. The structure and dynamics of G035.39–00.33 have been studied extensively, revealing the presence of multiple subfilaments that feed their embedded core population[17,26,45–48].

CMZ. The inner few hundred parsecs of the Milky Way contain approximately 3–5% of the Milky Way's molecular gas, a reservoir of $2-7 \times 10^7\,M_\odot$ of molecular material[23,49]. The physical conditions of the gas are extreme compared with those in the galaxy disks discussed above: the density[50–52], temperature[53,54], velocity dispersion[10,55], radiation field[56], pressure[57,58] and cosmic ray ionization rate[59] are larger by factors of a few to several orders of magnitude. The gas is distributed throughout several coherent streams spanning 250 km s⁻¹ in velocity and with projected lengths of the order 100–250 pc (refs. [10,60–62]).

G0.253+0.016. On small scales in the CMZ, we focus on the IRDC G0.253+0.016. With a mass of around $10^5\,M_\odot$ and an equivalent radius of just 2–3 pc, G0.253+0.016 is one of the densest molecular clouds in the Galaxy[50,63,64]. Despite this, G0.253+0.016 shows very few signatures of active star formation[65]. Although single-dish observations depict G0.253+0.016 as a single, coherent and centrally condensed molecular cloud[66], more recent work suggests that G0.253+0.016 is dynamically complex and hierarchically structured[11].

Observations and data. Here we describe the observations and data, summarizing the relevant information in Extended Data Fig. 1.

NGC 4321. We analyse CO (2–1) emission from NGC 4321 (M100) observed by ALMA as part of the pilot programme for the PHANGS-ALMA survey (A. K. Leroy et al., manuscript in preparation). These Cycle 3 (programme 2015.1.00956.S) observations covered the galaxy using ALMA's main array of 12 m telescopes, the 7 m telescopes from the Morita Atacama Compact Array and the total power dishes. The galaxy was covered by two large mosaics, which were observed separately. Data calibration used the standard ALMA pipeline. For imaging, we combined the data from the 12 m and 7 m arrays, carried out a multiscale deconvolution and then 'feathered' the interferometric images with the total power data to produce the final images. A first version of these maps initially appeared in ref. [67]. Sample selection, observing strategy, data reduction, imaging and post-processing are described in A. K. Leroy et al. (manuscript in preparation).

Relevant to this work, these data include total power and short spacing information and so have sensitivity to all spatial scales. For imaging, we binned the data to have a channel width of 2.5 km s⁻¹. During post-processing, two mosaics were convolved to share a matched ~1.6″ beam (~120 pc at the adopted distance to NGC 4321 of 15.2 Mpc; ref. [68]) and then linearly combined to form a single data cube covering most bright CO emission from the galaxy. Following ref. [67], ~70% of the total CO emission present in the target region is recovered at good signal to noise at 1.6″ resolution.

The Galactic Disk. We use data from the Boston University Five College Radio Astronomy Observatory (FCRAO) Galactic Ring Survey (GRS)[15]. This survey covered the lowest rotational transition of the ¹³CO isotopologue ($J=1{\to}0$) with an angular resolution of 46″, a pixel sampling of 22″ and a spectral resolution of 0.21 km s⁻¹. At a distance of 3 kpc, relevant for GMF 38.1–32.4b[36], the angular resolution of these data corresponds to a physical resolution of about 0.7 pc. The GRS covers a range in Galactic longitude, l, and latitude, b, of $14.0° < l < 56.0°$ and $-1.1° < b < 1.1°$. The region displayed in Fig. 1b thereby encloses both GMF 38.1–32.4b and G035.39–00.33 and covers $33.0° < l < 38.0°$, the full Galactic latitude coverage, and $25 \leq v_{LSR} \leq 70$ km s⁻¹. Note that because of our view through the Galactic Plane, this panel contains molecular gas situated at different distances, and GMF 38.1–32.4b comprises only a small fraction of these data (see the Data selection for statistical analysis section).

G035.39–00.33. We analyse N₂H⁺ (1–0) emission associated with G035.39–00.33 observed with the Institut de Radioastronomie Millimétrique (IRAM) Plateau de Bure Interferometer. These data were first presented in refs. [17,26]. The observations cover the northern portion of the cloud and have an angular extent of $40″ \times 150″$ ($0.6\,\mathrm{pc} \times 2.1\,\mathrm{pc}$; assuming a kinematic distance of 2.9 kpc; ref. [41]). These data were combined with IRAM-30m telescope observations first presented in ref. [45] to recover the zero-spacing information. The data are convolved to a circular beam of 5″ (the native spatial resolution is $3.9″ \times 3.2″$), corresponding to a physical resolution of 0.07 pc. In this study, we retain the native pixel scaling of 0.76″ (ref. [17] downsampled the data to 2″ pixels). The spectral resolution of the data is 0.14 km s⁻¹, and the sensitivity is of the order 1 mJy per beam. Further details of these observations and their combination are included in ref. [17].

CMZ. We use data from the Mopra CMZ survey[16]. These observations cover the region $-0.65° < l < 1.1°$ and $-0.25° < b < 0.20°$, which incorporates material within a galactocentric radius of approximately 125 pc (assuming a distance of 8,340 pc; ref. [69]). The spatial resolution of the observations is 60″, which corresponds to a physical resolution of 2.4 pc. The spectral resolution of the observations is 2 km s⁻¹. The data included in Fig. 1d show the HNC (1–0) emission analysed in ref. [10], which is extended over the entire CMZ. However, note that for our statistical study we use N₂H⁺ (1–0), consistent with ref. [13] (see the Spectral decomposition section). We refer the reader to refs. [10,16] for further discussion on these data.

The Herschel column density data was computed using modified blackbody fits to the HiGAL data[70], using the 160, 250, 350 and 500 μm bands (C. Battersby et al., manuscript in preparation). The 70 μm band was excluded from the fit due to possible contamination from very small, warm dust grains. At the wavelengths observed with Herschel, there is considerable contamination from Galactic cirrus emission, which was removed through an iterative process described in refs. [71,72]. All of the data were smoothed to the HiGAL reported beam size at the longest wavelength, 36″ (ref. [70]), and the maps are presented at this resolution.

G0.253+0.016. We include the ALMA Cycle 0 observations (programme 2011.0.00217.S) of IRDC G0.253+0.016 studied in detail by ref.[11]. These data were first presented in ref.[64]. The observations cover the full $180'' \times 60''$ (7.1 pc × 2.4 pc; assuming a distance of 8,340 pc; ref.[69]) extent of the molecular cloud. We focus exclusively on the HNCO $4(0,4) - 3(0,3)$ transition. These data were combined with single-dish observations from the The Millimeter Astronomy Legacy Team 90 GHz (MALT90) survey[73,74] to recover the zero-spacing information. The spatial resolution of the data is 1.7″, which corresponds to a physical resolution of 0.07 pc. The spectral resolution of the data is 3.4 km s⁻¹.

Spectral decomposition. In this section, we describe the spectral decomposition of the data discussed above. For an introduction to the methodology and a description of the techniques used, we refer the reader to the Supplementary Information. The spectral decomposition of the CMZ fields displayed in Fig. 1d,e is described in full in refs.[10,11], respectively. Although Fig. 1d shows the HNC $(1-0)$ decomposition to better highlight extended emission, we use the decomposition of N_2H^+ $(1-0)$ emission for the structure function analysis presented in Fig. 2d, consistent with ref.[13].

New to this work, we apply SCOUSEPY (version 1.0) to the CO $(2-1)$ data towards NGC 4321. We set the width of our Spectral Averaging Areas (SAAs) to 100 pixels, corresponding to about 1.8 kpc at the assumed distance of NGC 4321 (15.2 Mpc). A total of 1.1×10^5 model solutions were obtained out of the 2.3×10^5 included in the SAA coverage. A total of 1.2×10^5 Gaussian components were extracted during the fitting procedure, indicating that the models were mostly single-component fits. Multiple component fits were largely confined to the inner part of the Galaxy and a few concentrated regions in the spiral arms.

The decomposition of the Galactic disk region, focusing on GMF 38.1–32.4b[36], is performed using the machine learning algorithm GAUSSPY+ (version 0.2)[12] (see Supplementary Information). The details of the decomposition of the entire ¹³CO $(1-0)$ GRS dataset are described in full in ref.[75]. We train GAUSSPY with 12 training sets each containing 500 randomly chosen spectra from the GRS data set. These training sets are automatically generated with GAUSSPY+, and their decomposition was benchmarked against the training set functionality of SCOUSEPY[11], which takes randomly sampled regions of survey data for training set development. We find good agreement between the results of the two methods in these subregions, justifying our application of GAUSSPY+. Figure 1b shows a subsample of the GRS decomposition containing almost 3×10^5 components within $33° < l < 38°$, the full Galactic latitude coverage, and $25 \le v_{LSR} \le 70$ km s⁻¹.

For G035.39–00.33, the spectral decomposition is performed using SCOUSEPY and therefore differs from that originally presented in ref.[17]. We perform our Gaussian decomposition focusing exclusively on the isolated $F_1, F = 0,1 \rightarrow 1,2$, component of the $J = 1 \rightarrow 0$ transition of N_2H^+ at 93,176.2522 MHz (ref.[76]). We set the width of our SAAs to 16 pixels, corresponding to about 0.2 pc at the assumed distance of G035.39–00.33 (2.9 kpc). A total of 1.5×10^4 velocity components were fitted to 7×10^3 pixels, and multiple velocity components are required to describe the spectral line profiles over a significant (69%) portion of the map.

Data selection for statistical analysis. In the following section, we describe our data selection for the statistical analysis presented in Fig. 2. A potential source of uncertainty in interpreting the results from kinematic analysis methods is that observational data is sensitive only to estimators of the true underlying density and velocity fields. Spectral decomposition, which relies on the profile of emission lines, can be vulnerable to the influence of velocity crowding[77–79] and variations in optical depth. Fortunately, the influence of these effects can be mitigated through careful selection of environment and spectral lines.

We select subregions from each of the five environments discussed in the Environment selection section and presented in Fig. 1. We select three subregions, which, despite tracing vastly different scales, display similar morphology in that they are highly filamentary and (qualitatively) interspersed with quasiperiodic intensity peaks along their crests: part of the southern spiral arm in NGC 4321, part of the CMZ gas stream and a filament embedded within a GMC located in the Galactic Disk. We further select two GMCs, one in the Galactic Disk and one in the Milky Way's CMZ, the intensity profiles of which are complex and disordered. Our selected regions are displayed in Extended Data Fig. 2.

Spiral arm. For our analysis of NGC 4321, we select a region that shows a sample of regularly spaced infrared peaks[14]. These star-forming complexes, inferred by the presence of mid-infrared emission, are located within NGC 4321's southern spiral arm (see green crosses in fig. 4 of ref.[14]).

We expect that the influence of velocity crowding is minimized in this region by the limited molecular scale height of the galaxy, which is viewed face on. Similarly, although the CO $(2-1)$ is probably optically thick, single velocity components provide a suitable description for most of the CO $(2-1)$ emission along the arm. This indicates that our centroid measurements are not strongly influenced by optical depth effects. Where two velocity components are necessary to model the emission, the secondary component (that is, the one that appears in addition to the component most closely tracing the spiral arm) is often spatially localized and compact, of low brightness temperature and offset in velocity from the emission tracing the arm. We remove these additional components by

selecting the brightest velocity component at each location. We further select the molecular cloud complexes that follow the coherent structure of the spiral using GLUE[80,81]. Extended Data Fig. 2a shows the data that we have selected for our statistical analysis.

Galactic Disk GMC. The effect of velocity crowding is particularly pertinent in studies of the Milky Way, where our view through the Galactic Plane complicates our physical interpretation of $p-p-v$ space. Molecular clouds, coherent in true 3D space may be separated in $p-p-v$ space due to complex dynamics. Similarly, molecular clouds projected along the same line-of-sight, but otherwise physically decoupled, may crowd in $p-p-v$ space. These effects are expected to be most prominent towards the tangent point velocities of the Milky Way's rotation curve[75]. As GMF 38.1–32.4b is separated by around 40 km s⁻¹ from the tangent point velocity at $l = 35°$ (ref.[82]), we expect the effects of velocity crowding to be small.

The gas associated with GMF 38.1–32.4b makes up only a small fraction of the total emission displayed in Fig. 1b. To isolate this GMC from the sample of data shown in Fig. 1b, we use ACORNS[11], an n-dimensional unsupervised clustering algorithm designed for the analysis of spectroscopic $p-p-v$ data[11]. We apply ACORNS directly to the data shown in Fig. 1b. We cluster the data on the basis of position, centroid velocity and the velocity dispersion information provided by our decomposition. From the resulting hierarchy of clusters, we identify the cluster that most closely matches the morphology of GMF 38.1–32.4b as identified by ref.[36]. The result of this analysis is displayed in Extended Data Fig. 2b, where we show the peak brightness temperature of the ¹³CO $(1-0)$ emission of the ACORNS cluster. Our ACORNS-identified cluster shows excellent agreement with the GMF extracted in ref.[36], which is highlighted by the white contour.

GMC filament. The association between GMF 38.1–32.4b and IRDC G035.39–00.33 is evident in Extended Data Fig. 2b, where G035.39–00.33 is identified as a compact, bright source of ¹³CO $(1-0)$ emission. We apply ACORNS to our new decomposition of the N_2H^+ $(1-0)$ data. Our clustering analysis is consistent with the results of ref.[17] in that the N_2H^+ $(1-0)$ emission is mainly distributed throughout three dominant subfilaments (see also ref.[48]). This high-density gas tracer is less susceptible to the effects of velocity crowding and line-of-sight confusion[83]. Furthermore, the isolated hyperfine component of N_2H^+ $(1-0)$ is measured to be optically thin[17]. The subfilament selected for our structure function analysis is shown in Extended Data Fig. 2c. The filament exhibits strong, localized velocity fluctuations along its primary axis (evident in Fig. 1c).

CMZ. As proof of concept of our statistical analysis, we reanalyse the region of the CMZ studied by ref.[13]. In general, the effects of velocity crowding are less prominent in the CMZ, where the gas is distributed throughout molecular streams that are well separated in velocity[10,62]. Our selected region is located between $-0.65° < l < 0.0°$ and $-0.05° < b < 0.1°$, and is associated both with a series of quasiregularly spaced molecular cloud condensations and an oscillatory pattern in the centroid velocity of the molecular gas. This velocity pattern is observed in multiple tracers[10,13,84,85], indicating that it is of dynamical origin, and not simply the result of excitation or optical depth effects. Extended Data Fig. 2d displays the Herschel-derived column density map (C. Battersby et al., manuscript in preparation) covering the region that displays the coherent velocity oscillation investigated in ref.[13]. These data were selected using the software GLUE[80,81], using the location of the centroid velocity measurements from ref.[13] as a guide for masking.

CMZ GMC. We focus our analysis on one of the dominant substructures of G0.253+0.016, extracted using ACORNS[11]. The distribution of optically thin[11] emission from the $4(0,4) - 3(0,3)$ transition of HNCO throughout our selected substructure, labelled 'tree C' in ref.[11], is morphologically similar to that of the dust continuum emission associated with the cloud. This structure therefore probably dominates the internal physical composition of G0.253+0.016. The HNCO $4(0,4) - 3(0,3)$ emission profile of this substructure is displayed in the bottom-right panel of Extended Data Fig. 2e.

Statistical analysis of the observational data. In the following section, we discuss our statistical analysis of our selected subregions. We group the subregions according to their dominant geometry: either long and filamentary or multidimensional and complex. The physical interpretation of the following analysis is discussed at length in the Summary of the results and physical interpretation section of the Supplementary Information.

Analysis of filamentary structures. We perform our analysis along the crests of each subregion. We obtain the crest of each filamentary structure by applying FILFINDER[86] to our selected density tracer in each environment, CO $(2-1)$ in the spiral arm, the Herschel-derived column density map in the CMZ and the N_2H^+ $(1-0)$ emission in the GMC filament (see Extended Data Fig. 2).

We perform a weighted mean of our selected density tracer (weighting by the square of the Gaussian fit amplitude value) orthogonal to the crest. The resulting profiles (solid) and the standard deviation about the mean (shaded region) are shown in the top panels of Extended Data Fig. 3.

For the velocity field, we remove the bulk motion by modelling it with a simple polynomial function and subtracting this model from the velocity field derived from our spectral decomposition, leaving only the residual local velocity fluctuations. We measure a weighted mean velocity (weighting by the square of the Gaussian fit amplitude value) orthogonal to the crest. The resulting distributions (solid line) and the standard deviation about the mean (shaded region) are shown in the bottom panels of Extended Data Fig. 3.

We compute the one-dimensional (1D) structure function, S_p, on the data presented in Extended Data Fig. 3 using

$$S_p(\ell) = \langle \delta x(\mathbf{r}, \ell)^p \rangle = \langle |x(\mathbf{r}) - x(\mathbf{r} + \ell)|^p \rangle, \tag{1}$$

where the quantity $\delta x(\mathbf{r}, \ell)$ represents the absolute difference in the quantity x measured between two locations, $\mathbf{r}$ and $\mathbf{r} + \ell$ separated by lag ℓ. The structure function, $S_p(\ell)$, averages this quantity (raised to the pth power, the order) over all locations (indicated by the angle brackets). For a more comprehensive description of the structure function and its behaviour we refer the reader to the Structure functions and their application to toy models section in the Supplementary Information.

As the structure function compares pairs of points at a given ℓ, the maximum, fully sampled lag that fits within these 1D datasets is half of the total length of each crest. This defines our upper limit to the spatial scales over which the structure functions presented in Fig. 2 are computed. We generate noise-corrected structure functions by computing the structure function of the measurement uncertainties associated with our Gaussian fit components and subtracting this from the structure functions of the signal. A comprehensive description of the behaviour of the structure function in response to instrumental noise is included in the Supplementary Information. The results of this analysis are shown in Fig. 2.

We estimate the uncertainty on the structure function as

$$\sigma_{S_2}(\ell) = \frac{\sigma(\ell)}{\sqrt{N_{\text{indep}}}} \tag{2}$$

where σ represents the standard deviation of the measurements obtained at a given ℓ and N_{indep} is the number of independent measurements of S_2 taken at that same value of ℓ.

Each of the structure functions relating to our filamentary structures displays local minima at specific spatial scales. For our density tracers (dashed lines), these minima occur at spatial scales of $\lambda_\rho = 366^{+88}_{-77}$ pc in the spiral arm, both $6.0^{+0.8}_{-0.6}$ pc and $21.8^{+5.5}_{-6.3}$ pc in the CMZ and $0.32^{+0.01}_{-0.01}$ pc in the GMC filament (Table 1). The uncertainties on each of these measurements represent the full-width at half-minimum for each of the minima detected in the structure function. Periodicity in the density structure indicates that density enhancements are forming with a preferred, or characteristic, spacing. The structure function therefore provides a quantitative measure of the periodicity that is qualitatively evident in the maps presented in Extended Data Fig. 2. We demonstrate the response of the structure function to periodicity using toy models in the Supplementary Information (see Supplementary Fig. 1 for an example).

We compute the beam-deconvolved diameters of the filamentary structures for comparison with the above derived characteristic spacing. To do this, we use FilFinder[86] to compute radial intensity profiles normal to the spines identified above. We fit the radial profile with a Gaussian model with a mean centred on the filament spine and a constant background. The model is then deconvolved with the beam of the observations. For the spiral arm, CMZ stream and GMC filament we measure beam-deconvolved diameters of $D = 122 \pm 5$ pc, 4.2 ± 0.2 pc and 0.107 ± 0.001 pc, respectively; the characteristic wavelengths derived above are therefore of the order 3, 5 and 3 times the diameters of their parent structures, respectively.

Perhaps a more surprising feature of structure functions presented in Fig. 2 is that the velocity fluctuations along the crests of our selected regions also display periodic behaviour. Moreover, the characteristic wavelengths of the velocity fluctuations in each environment agree, within the uncertainties, with the periodicity detected in density. We measure the location of the minima in the velocity structure functions (solid lines) to be $\lambda_v = 405^{+92}_{-76}$ pc for the spiral arm, $22.0^{+5.4}_{-6.3}$ pc for the CMZ and $0.28^{+0.06}_{-0.08}$ pc in the GMC filament (Table 1).

To assess the phase relationship between density (ρ) and velocity (v) fluctuations, we introduce the cross-correlation, which is defined

$$\text{XC}(\ell) = \langle \rho(\mathbf{r}) v(\mathbf{r} + \ell) \rangle. \tag{3}$$

XC tells us how closely related the density and velocity fields are as a function of displacement, or ℓ, relative to one another.

We define the associated uncertainty in the XC function as

$$\sigma_{\text{XC}}^2(\ell) = \Sigma_{\mathbf{r}} \left[\sigma_{\rho(\mathbf{r})}^2 v(\mathbf{r} + \ell)^2 \right] + \Sigma_{\mathbf{r}} \left[\sigma_{v(\mathbf{r}+\ell)}^2 \rho(\mathbf{r})^2 \right] \tag{4}$$

where σ_ρ and σ_v represent the standard deviation of our measurements (shown as the coloured shaded regions in Extended Data Fig. 3). Given that both variables (density and velocity) exhibit periodicity in each of our subregions, and are therefore autocorrelated, the XC function has multiple peaks at different lags. We

therefore identify all significant ($\text{XC}(\ell)/\sigma_{\text{XC}}(\ell)) > 3$) peaks in the XC function, and select the one that is located at the smallest ℓ, as the representative phase-shift between density and velocity.

We measure phase differences between density and velocity of 191 ± 62 pc for the spiral arm, 2.7 ± 2.9 pc for the CMZ and 0.11 ± 0.03 pc for the GMC filament, respectively. The uncertainty in each of these measurements represents the standard deviation of a Gaussian fitted to the relevant peaks in the XC function.

Given that the spatial resolution of our density (column density from Herschel) and velocity (N_2H^+ (1−0) emission from Mopra) tracers in the CMZ differ by a factor of two, we also compute the phase difference between density peaks and the velocity oscillations both derived from the N_2H^+ (1−0) emission and find 1.4 ± 2.9 pc (the emission profile of the N_2H^+ data is displayed in Extended Data Fig. 4b). Relative to the characteristic wavelengths derived for the velocity oscillations, λ_v, these phase differences are approximately $\lambda_v/2$ for the spiral arm, $\lambda_v/8$ ($\lambda_v/16$, for the N_2H^+ (1−0) emission) for the CMZ and $2\lambda_v/5$ for the GMC filament, respectively.

Analysis of multidimensional structures. The emission associated with the GMCs selected in our study do not follow a simple linear morphology (see Extended Data Fig. 2b,e). Owing to the lack of a dominant geometry, the structure functions presented in Fig. 2b,e are computed in two dimensions, thereby averaging the density and velocity fluctuations over all azimuthal angles in each GMC.

We generate noise-corrected structure functions by computing the structure function of the measurement uncertainties associated with our Gaussian fit components and subtracting this from the structure functions of the signal (see Supplementary Information). The structure functions presented in Fig. 2b,e display power-law behaviour over a limited spatial scale, consistent with scale-free fluctuations in both density (dashed lines) and velocity (solid lines). On large scales, the structure functions begin to flatten due to insufficient sampling[87] (see Fig. 2). We fit the structure functions with power-law functions of the form $S_s(\ell) \propto \ell^{\zeta_2}$. We set the lower and upper limits of our fitting range to the beam size[88] (0.65 pc and 0.07 pc for the GMCs in the disk and CMZ, respectively) and the approximate scale above which the structure functions begin to turn over (4 pc and 0.7 pc for the GMCs in the disk and CMZ, respectively).

We find that the structure functions of density for our GMCs in the disk and CMZ increase with increasing spatial scale with scaling exponents $\zeta_2 = 0.82 \pm 0.03$ and 0.91 ± 0.01. Similarly, we measure scaling exponents for the velocity structure functions of $\zeta_2 = 0.82 \pm 0.02$ and $\zeta_2 = 0.74 \pm 0.01$, respectively.

We also investigate whether the scaling between the velocity structure functions and spatial scale differs as a function of direction. We compute the structure functions as a function of azimuthal angle in 10° increments between 0° (Galactic east–west) and 90° (Galactic north–south). We measure mean scaling exponents of $\zeta_2 = 0.76 \pm 0.03$ and $\zeta_2 = 0.72 \pm 0.02$ (where the uncertainty represents the standard deviation of the measurements), for the GMCs in the disk and CMZ, respectively. The small standard deviations of these measurements indicate that the velocity fluctuations have no preferred orientation. We find tentative evidence for a trend between our measured scaling exponents and increasing azimuthal angle in our CMZ GMC ($R^2 = 0.67$, $P = 0.003$). No such trend is evident for our selected GMC in the Galactic Disk.

Data availability

The ^{13}CO (1−0) data of the Galactic Disk are from the Boston University-FCRAO GRS. The GRS data are publicly available at https://www.bu.edu/galacticring/new_data.html. The Mopra data are publicly available at http://newt.phys.unsw.edu.au/mopracmz/data.html. The ALMA HNCO 4(0,4) − 3(0,3) data of G0.253+0.016 are from project 2011.0.00217.S (principal investigator: J. Rathborne) and the raw data are publicly available through the ALMA archive (https://almascience.eso.org/alma-data/archive). All other data that support the findings of this study are available from the corresponding author on reasonable request. Source data are provided with this paper.

Code availability

SCOUSEPY and ACORNS, as well as the codes used for our statistical analyses, are freely available at https://github.com/jdhenshaw. GAUSSPY+ is available at https://github.com/mriener/gausspyplus. Assistance with this software can be provided by the corresponding author.

References

1. McKee, C. F. & Ostriker, E. C. Theory of star formation. *Annu. Rev. Astron. Astrophys.* **45**, 565–687 (2007).
2. Zinnecker, H. & Yorke, H. W. Toward understanding massive star formation. *Annu. Rev. Astron. Astrophys.* **45**, 481–563 (2007).
3. Naab, T. & Ostriker, J. P. Theoretical challenges in galaxy formation. *Annu. Rev. Astron. Astrophys.* **55**, 59–109 (2017).

4. Kruijssen, J. M. D. et al. Fast and inefficient star formation due to short-lived molecular clouds and rapid feedback. *Nature* **569**, 519–522 (2019).

5. Dobbs, C. L. et al. in *Protostars Planets VI* (eds. H. Beuther et al.) 3–26 (Univ. of Arizona Press, 2014).

6. Elmegreen, B. G. & Elmegreen, D. M. Regular strings of H II regions and superclouds in spiral galaxies - clues to the origin of cloudy structure. *Mon. Not. R. Astron. Soc.* **203**, 31–45 (1983).

7. Kim, W.-T., Ostriker, E. C. & Stone, J. M. Magnetorotationally driven galactic turbulence and the formation of giant molecular clouds. *Astrophys. J.* **599**, 1157–1172 (2003).

8. Vázquez-Semadeni, E., Palau, A., Ballesteros-Paredes, J., Gómez, G. C. & Zamora-Avilés, M. Global hierarchical collapse in molecular clouds. towards a comprehensive scenario. *Mon. Not. R. Astron. Soc.* **490**, 3061–3097 (2019).

9. Padoan, P. et al. in *Protostars Planets VI* (eds. H. Beuther et al.) 77–100 (Univ. of Arizona Press, 2014).

10. Henshaw, J. D. et al. Molecular gas kinematics within the central 250 pc of the Milky Way. *Mon. Not. R. Astron. Soc.* **457**, 2675–2702 (2016).

11. Henshaw, J. D. et al. 'The Brick' is not a brick: a comprehensive study of the structure and dynamics of the central molecular zone cloud G0.253+0.016. *Mon. Not. R. Astron. Soc.* **485**, 2457–2485 (2019).

12. Riener, M. et al. GAUSSPY+: A fully automated Gaussian decomposition package for emission line spectra. *Astron. Astrophys.* **628**, A78 (2019).

13. Henshaw, J. D., Longmore, S. N. & Kruijssen, J. M. D. Seeding the galactic centre gas stream: gravitational instabilities set the initial conditions for the formation of protocluster clouds. *Mon. Not. R. Astron. Soc.* **463**, L122–L126 (2016).

14. Elmegreen, B. G., Elmegreen, D. M. & Efremov, Y. N. Regularly spaced infrared peaks in the dusty spirals of messier 100. *Astrophys. J.* **863**, 59 (2018).

15. Jackson, J. M. et al. The boston university-five college radio astronomy observatory galactic ring survey. *Astrophys. J. Suppl.* **163**, 145–159 (2006).

16. Jones, P. A. et al. Spectral imaging of the central molecular zone in multiple 3-mm molecular lines. *Mon. Not. R. Astron. Soc.* **419**, 2961–2986 (2012).

17. Henshaw, J. D., Caselli, P., Fontani, F., Jiménez-Serra, I. & Tan, J. C. The dynamical properties of dense filaments in the infrared dark cloud G035.39-00.33. *Mon. Not. R. Astron. Soc.* **440**, 2860–2881 (2014).

18. Klessen, R. S. & Hennebelle, P. Accretion-driven turbulence as universal process: galaxies, molecular clouds, and protostellar disks. *Astron. Astrophys.* **520**, A17 (2010).

19. Tafalla, M. & Hacar, A. Chains of dense cores in the taurus L1495/B213 complex. *Astron. Astrophys.* **574**, A104 (2015).

20. Lang, P. et al. PHANGS CO kinematics: disk orientations and rotation curves at 150 pc resolution. *Astrophys. J.* (in the press).

21. Elmegreen, B. G., Elmegreen, D. M. & Seiden, P. E. Spiral-arm amplitude variations and pattern speeds in the grand design galaxies M51, M81, and M100. *Astrophys. J.* **343**, 602–607 (1989).

22. Meidt, S. E. et al. Gas kinematics on giant molecular cloud scales in M51 with PAWS: cloud stabilization through dynamical pressure. *Astrophys. J.* **779**, 45 (2013).

23. Heyer, M. & Dame, T. M. Molecular clouds in the Milky Way. *Annu. Rev. Astron. Astrophys.* **53**, 583–629 (2015).

24. Larson, R. B. Turbulence and star formation in molecular clouds. *Mon. Not. R. Astron. Soc.* **194**, 809–826 (1981).

25. André, P. et al. in *Protostars Planets VI* (eds. H. Beuther et al.) 27–51 (Univ. of Arizona Press, 2014).

26. Henshaw, J. D. et al. Investigating the structure and fragmentation of a highly filamentary IRDC. *Mon. Not. R. Astron. Soc.* **463**, 146–169 (2016).

27. Misugi, Y., Inutsuka, S.-i & Arzoumanian, D. An origin for the angular momentum of molecular cloud cores: a prediction from filament fragmentation. *Astrophys. J.* **881**, 11 (2019).

28. Schneider, S. & Elmegreen, B. G. A catalog of dark globular filaments. *Astrophys. J. Suppl.* **41**, 87–95 (1979).

29. Elmegreen, B. G. Supercloud formation by gravitational collapse of magnetic gas in the crest of a spiral density wave. *Astrophys. J.* **433**, 39–47 (1994).

30. Nagasawa, M. Gravitational instability of the isothermal gas cylinder with an axial magnetic field. *Progr. Theor. Phys.* **77**, 635–652 (1987).

31. Inutsuka, S.-I. & Miyama, S. M. Self-similar solutions and the stability of collapsing isothermal filaments. *Astrophys. J.* **388**, 392–399 (1992).

32. de Vaucouleurs, G. et al. *Third Reference Catalogue of Bright Galaxies* (Springer, 1991).

33. Elmegreen, D. M. et al. Grand design and flocculent spirals in the Spitzer survey of stellar structure in galaxies (S^{4}G). *Astrophys. J.* **737**, 32 (2011).

34. Knapen, J. H., Beckman, J. E., Heller, C. H., Shlosman, I. & de Jong, R. S. The central region in M100: observations and modeling. *Astrophys. J.* **454**, 623 (1995).

35. Knapen, J. H., Beckman, J. E., Cepa, J. & Nakai, N. Molecular gas observations and enhanced massive star formation efficiencies in M100. *Astron. Astrophys.* **308**, 27–39 (1996).

36. Ragan, S. E. et al. Giant molecular filaments in the Milky Way. *Astron. Astrophys.* **568**, A73 (2014).

37. Goodman, A. A. et al. The bones of the Milky Way. *Astrophys. J.* **797**, 53 (2014).

38. Zucker, C., Battersby, C. & Goodman, A. The skeleton of the Milky Way. *Astrophys. J.* **815**, 23 (2015).

39. Abreu-Vicente, J. et al. Giant molecular filaments in the Milky Way. II: the fourth galactic quadrant. *Astron. Astrophys.* **590**, A131 (2016).

40. Zucker, C., Battersby, C. & Goodman, A. Physical properties of large-scale galactic filaments. *Astrophys. J.* **864**, 153 (2018).

41. Simon, R., Rathborne, J. M., Shah, R. Y., Jackson, J. M. & Chambers, E. T. The characterization and galactic distribution of infrared dark clouds. *Astrophys. J.* **653**, 1325–1335 (2006).

42. Kainulainen, J. & Tan, J. C. High-dynamic-range extinction mapping of infrared dark clouds: dependence of density variance with sonic Mach number in molecular clouds. *Astron. Astrophys.* **549**, A53 (2013).

43. Jiménez-Serra, I. et al. Parsec-scale SiO emission in an infrared dark cloud. *Mon. Not. R. Astron. Soc.* **406**, 187–196 (2010).

44. Nguyên Luong, Q. et al. The *Herschel* view of massive star formation in G035.39-00.33: dense and cold filament of W48 undergoing a mini-starburst. *Astron. Astrophys.* **535**, A76 (2011).

45. Henshaw, J. D. et al. Complex, quiescent kinematics in a highly filamentary infrared dark cloud. *Mon. Not. R. Astron. Soc.* **428**, 3425–3442 (2013).

46. Henshaw, J. D. et al. Unveiling the early-stage anatomy of a protocluster hub with ALMA. *Mon. Not. R. Astron. Soc.* **464**, L31–L35 (2017).

47. Jiménez-Serra, I. et al. Gas kinematics and excitation in the filamentary IRDC G035.39-00.33. *Mon. Not. R. Astron. Soc.* **439**, 1996–2013 (2014).

48. Sokolov, V. et al. Multicomponent kinematics in a massive filamentary infrared dark cloud. *Astrophys. J.* **872**, 30 (2019).

49. Ferrière, K., Gillard, W. & Jean, P. Spatial distribution of interstellar gas in the innermost 3 kpc of our galaxy. *Astron. Astrophys.* **467**, 611–627 (2007).

50. Longmore, S. N. et al. G0.253 + 0.016: a molecular cloud progenitor of an arches-like cluster. *Astrophys. J.* **746**, 117 (2012).

51. Longmore, S. N. et al. Variations in the galactic star formation rate and density thresholds for star formation. *Mon. Not. R. Astron. Soc.* **429**, 987–1000 (2013).

52. Mills, E. A. C. et al. The dense gas fraction in galactic center clouds. *Astrophys. J.* **868**, 7 (2018).

53. Ginsburg, A. et al. Dense gas in the galactic central molecular zone is warm and heated by turbulence. *Astron. Astrophys.* **586**, A50 (2016).

54. Krieger, N. et al. The survey of water and ammonia in the galactic center (swag): molecular cloud evolution in the central molecular zone. *Astrophys. J.* **850**, 77 (2017).

55. Shetty, R., Beaumont, C. N., Burton, M. G., Kelly, B. C. & Klessen, R. S. The linewidth-size relationship in the dense interstellar medium of the central molecular zone. *Mon. Not. R. Astron. Soc.* **425**, 720–729 (2012).

56. Clark, P. C., Glover, S. C. O., Ragan, S. E., Shetty, R. & Klessen, R. S. On the temperature structure of the galactic center cloud G0.253+0.016. *Astrophys. J. Lett.* **768**, L34 (2013).

57. Kruijssen, J. M. D. & Longmore, S. N. Comparing molecular gas across cosmic time-scales: the Milky Way as both a typical spiral galaxy and a high-redshift galaxy analogue. *Mon. Not. R. Astron. Soc.* **435**, 2598–2603 (2013).

58. Walker, D. L. et al. Star formation in a high-pressure environment: an SMA view of the galactic centre dust ridge. *Mon. Not. R. Astron. Soc.* **474**, 2373–2388 (2018).

59. Yusef-Zadeh, F., Muno, M., Wardle, M. & Lis, D. C. The origin of diffuse X-ray and γ-ray emission from the galactic center region: cosmic-ray particles. *Astrophys. J.* **656**, 847–869 (2007).

60. Sofue, Y. Galactic-center molecular arms, ring, and expanding shell. I: kinematical structures in longitude-velocity diagrams. *Publ. Astron. Soc. Jpn* **47**, 527–549 (1995).

61. Molinari, S. et al. A 100 pc elliptical and twisted ring of cold and dense molecular clouds revealed by Herschel around the galactic center. *Astrophys. J. Lett.* **735**, L33 (2011).

62. Kruijssen, J. M. D., Dale, J. E. & Longmore, S. N. The dynamical evolution of molecular clouds near the galactic centre. I: orbital structure and evolutionary timeline. *Mon. Not. R. Astron. Soc.* **447**, 1059–1079 (2015).

63. Kauffmann, J., Pillai, T. & Zhang, Q. The galactic center cloud G0.253.0.016: a massive dense cloud with low star formation potential. *Astrophys. J. Lett.* **765**, L35 (2013).

64. Rathborne, J. M. et al. A cluster in the making: ALMA reveals the initial conditions for high-mass cluster formation. *Astrophys. J.* **802**, 125 (2015).

65. Mills, E. A. C. et al. Abundant CH$_3$ OH masers but no new evidence for star formation in GCM0.253+0.016. *Astrophys. J.* **805**, 72 (2015).

66. Rathborne, J. M. et al. G0.253+0.016: a centrally condensed, high-mass protocluster. *Astrophys. J.* **786**, 140 (2014).

67. Sun, J. et al. Cloud-scale molecular gas properties in 15 nearby galaxies. *Astrophys. J.* **860**, 172 (2018).

68. Tully, R. B. et al. The extragalactic distance database. *Astron. J.* **138**, 323–331 (2009).
69. Reid, M. J. et al. Trigonometric parallaxes of high mass star forming regions: the structure and kinematics of the Milky Way. *Astrophys. J.* **783**, 130 (2014).
70. Molinari, S. et al. Clouds, filaments, and protostars: the Herschel Hi-GAL Milky Way. *Astron. Astrophys.* **518**, L100 (2010).
71. Battersby, C. et al. Characterizing precursors to stellar clusters with Herschel. *Astron. Astrophys.* **535**, A128 (2011).
72. Mills, E. A. C. & Battersby, C. Origins of scatter in the relationship between HCN 1-0 and dense gas mass in the galactic center. *Astrophys. J.* **835**, 76 (2017).
73. Foster, J. B. et al. The Millimetre Astronomy Legacy Team 90 GHz (MALT90) pilot survey. *Astrophys. J. Suppl.* **197**, 25 (2011).
74. Jackson, J. M. et al. MALT90: the Millimetre Astronomy Legacy Team 90 GHz survey. *Publ. Astron. Soc. Aus.* **30**, e057 (2013).
75. Riener, M. et al. Autonomous gaussian decomposition of the galactic ring survey. I: global statistics and properties of the ^{13}CO emission data. *Astron. Astrophys.* **633**, A14 (2020).
76. Pagani, L., Daniel, F. & Dubernet, M. L. On the frequency of N_2H^+ and N_2D^+. *Astron. Astrophys.* **494**, 719–727 (2009).
77. Burton, W. B. On the kinematic distribution of galactic neutral hydrogen. *Astron. Astrophys.* **19**, 51–65 (1972).
78. Lazarian, A. & Pogosyan, D. Velocity modification of H I power spectrum. *Astrophys. J.* **537**, 720–748 (2000).
79. Ostriker, E. C., Stone, J. M. & Gammie, C. F. Density, velocity, and magnetic field structure in turbulent molecular cloud models. *Astrophys. J.* **546**, 980–1005 (2001).
80. Beaumont, C., Goodman, A. & Greenfield, P. in *Astronomical Data Analysis Software and Systems XXIV* (eds Taylor, A. R. & Rosolowsky, E.) 101–110 (Astronomical Society of the Pacific, 2015).
81. Robitaille, T., Beaumont, C., Qian, P., Borkin, M. & Goodman, A. glueviz v0.13.1: multidimensional data exploration (2017); https://doi.org/10.5281/zenodo.1237692
82. Reid, M. J. et al. Trigonometric parallaxes of high-mass star-forming regions: our view of the Milky Way. *Astrophys. J.* **885**, 131 (2019).
83. Clarke, S. D. et al. Synthetic C ^{18}O observations of fibrous filaments: the problems of mapping from PPV to PPP. *Mon. Not. R. Astron. Soc* **479**, 1722–1746 (2018).
84. Langer, W. D., Velusamy, T., Morris, M. R., Goldsmith, P. F. & Pineda, J. L. Kinematics and properties of the central molecular zone as probed with [C II]. *Astron. Astrophys.* **599**, A136 (2017).
85. Longmore, S. N. et al. H_2O southern galactic plane survey (HOPS): paper III—properties of dense molecular gas across the inner Milky Way. *Mon. Not. R. Astron. Soc.* **470**, 1462–1490 (2017).
86. Koch, E. W. & Rosolowsky, E. W. Filament identification through mathematical morphology. *Mon. Not. R. Astron. Soc.* **452**, 3435–3450 (2015).
87. Ossenkopf, V. & MacLow, M. M. Turbulent velocity structure in molecular clouds. *Astron. Astrophys.* **390**, 307–326 (2002).
88. Koch, E. W. et al. Spatial power spectra of dust across the local group: no constraint on disc scale height. *Mon. Not. R. Astron. Soc.* **492**, 2663–2682 (2020).

Acknowledgements

Author contributions

J.D.H., J.M.D.K. and S.N.L. were responsible for the experiment design. J.D.H. led the project, carried out the experiment, developed the analysis methods, interpreted the results and wrote the text, to which J.M.D.K, S.N.L. and M.R. contributed. E.R. created the mock datasets and designed the observational estimator 2D model test. J.D.H. and M.R. were responsible for data visualization. Supplementary Videos 1–5 were coproduced by J.D.H. Supplementary Videos 6–10 were produced by M.R. J.D.H. performed the spectral decomposition for all regions except for the GRS data for which M.R. was responsible. All authors contributed to aspects of the data reduction and analysis, the interpretation of the results, and the writing of the manuscript.

Competing interests

The authors declare no competing interests.

Additional information

Extended data is available for this paper at https://doi.org/10.1038/s41550-020-1126-z.

Supplementary information is available for this paper at https://doi.org/10.1038/s41550-020-1126-z.

Correspondence and requests for materials should be addressed to J.D.H.

Peer review information *Nature Astronomy* thanks Mark Heyer and Alex Lazarian for their contribution to the peer review of this work.

Reprints and permissions information is available at www.nature.com/reprints.

Publisher's note Springer Nature remains neutral with regard to jurisdictional claims in published maps and institutional affiliations.

Environment	ID/Region	Tracer	Distance	Resolution	Scales Probed
Nearby galaxy	NGC 4321	CO $(2-1)$	15.2 Mpc	$1\rlap{.}{''}6$	$10^2 - 10^3$ pc
Galactic disc	$33° < l < 38°, -1.1° < b < 1.1°$	^{13}CO $(1-0)$	[3.0 kpc]	$46''$	$[10^0 - 10^2$ pc]
Galactic disc GMC	G035.39–00.33	N_2H^+ $(1-0)$	2.9 kpc	$5''$	$10^{-1} - 10^1$ pc
CMZ	$-0\rlap{.}°65 < l < 1\rlap{.}°1, -0\rlap{.}°25 < b < 0\rlap{.}°2$	HNC $(1-0)$	8.2 kpc	$60''$	$10^0 - 10^2$ pc
CMZ GMC	G0.253+0.016	HNCO $4(0,4) - 3(0,3)$	8.2 kpc	$1\rlap{.}{''}7$	$10^{-1} - 10^1$ pc

Extended Data Fig. 1 | Summary of the observations. Here we highlight the observations and region selection for the data presented in Figure 1. The scales probed by our Galactic disc selection (seen in square brackets) are relevant for a distance of 3 kpc. Out of each of these environments we select sub-regions for the statistical analysis presented in Fig. 2 (see Statistical analysis of the observational data).
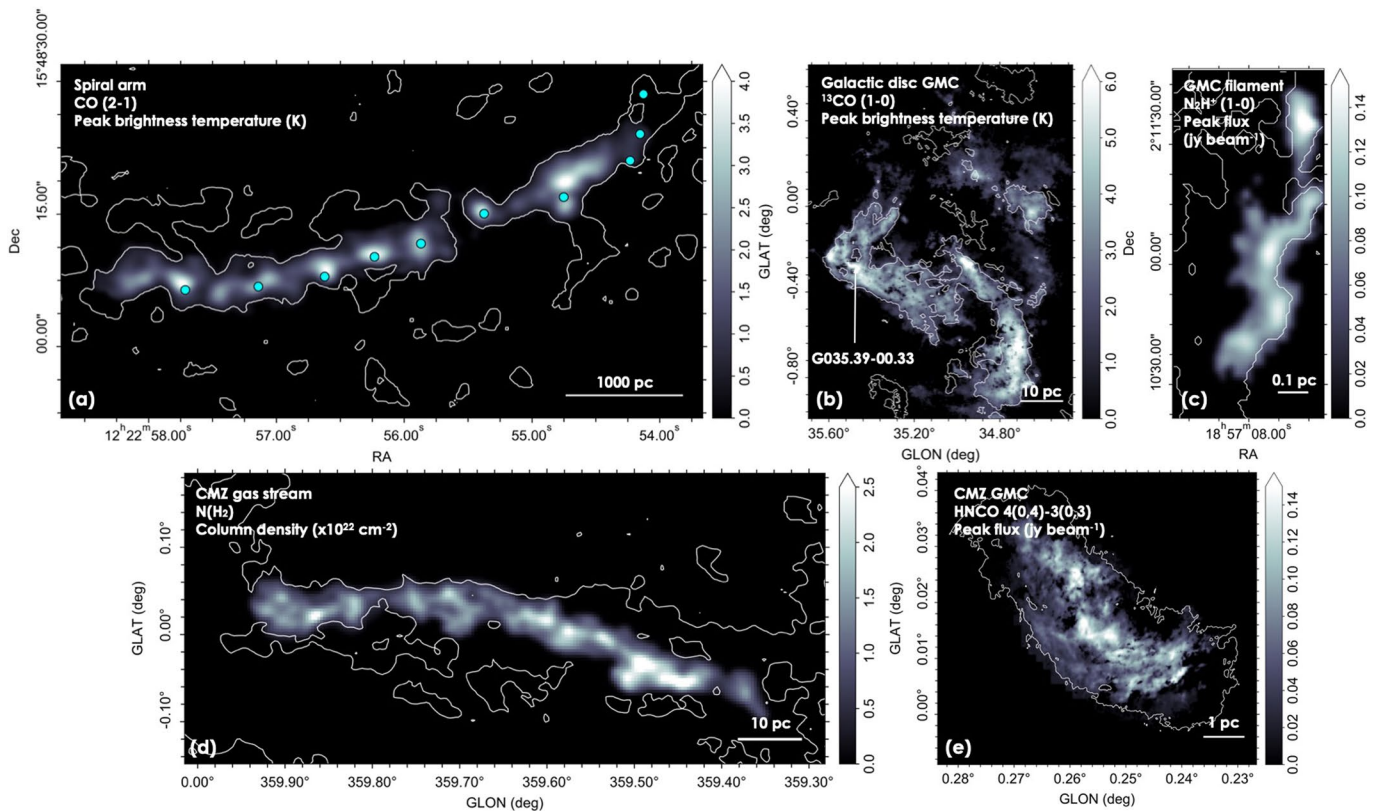
Extended Data Fig. 2 | Maps of the regions selected for statistical analysis. The upper panels display our galactic disc environments. From left to right we show part of the main southern spiral arm in NGC 4321 (**a**), a GMC in the Galactic disc (**b**), and an individual filament located within that same GMC (**c**). The bottom panels display our selected regions in the CMZ: The series of molecular clouds investigated by ref. [13] (**d**) and an individual GMC located within the CMZ gas stream (**e**). The cyan points in panel 'a' refer to the locations of star forming complexes identified in the mid-infrared[14]. In the upper left of each panel we indicate the tracer used to create each image. Scale bars are included in the bottom right corner of each image. These regions correspond to the areas over which we perform our statistical analysis (see Statistical analysis of the observational data and Fig. 2).
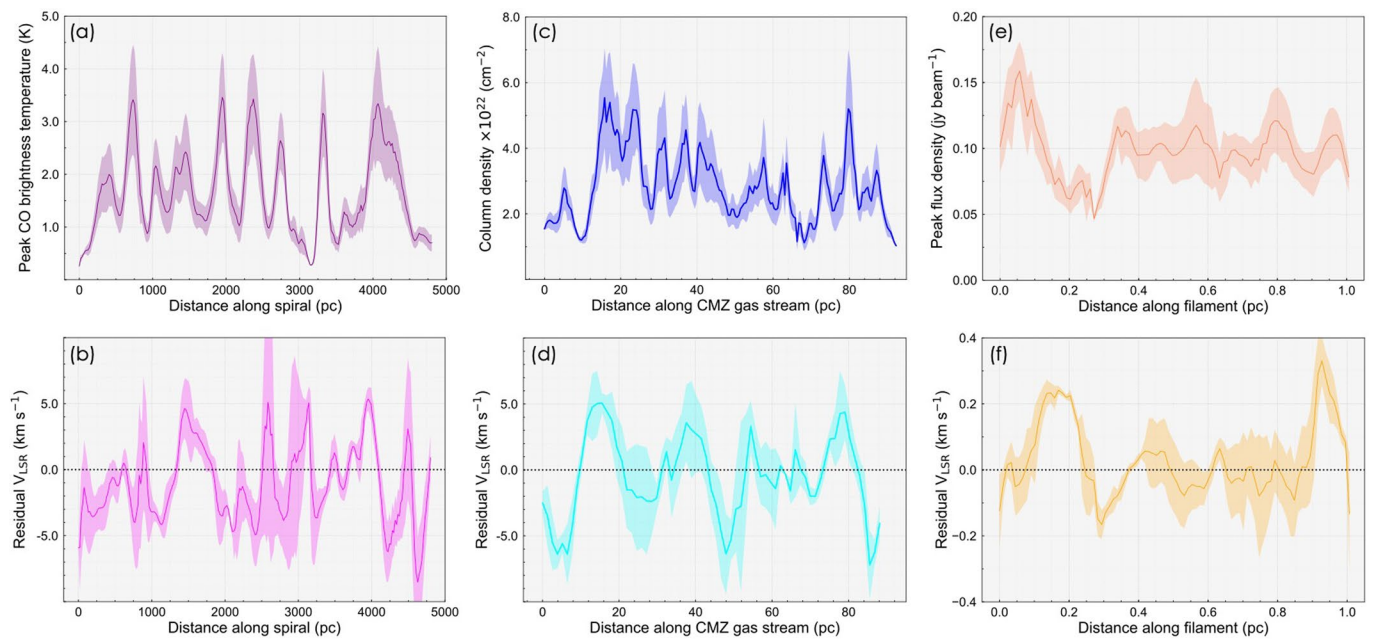
Extended Data Fig. 3 | Distribution of our density proxy (top) and velocity centroids (bottom) along the crest of the structures displaying periodicity. From left to right we show distance along the crest of each structure versus mean density (top) and velocity (bottom), for our selected regions in NGC 4321 (**a**, **b**), the CMZ (**c**, **d**), and IRDC G035.39-00.33 (**e**, **f**), respectively (see Extended Data Fig. 2). The coloured shaded region in each panel represents the standard deviation of the data measured orthogonal to the crest.
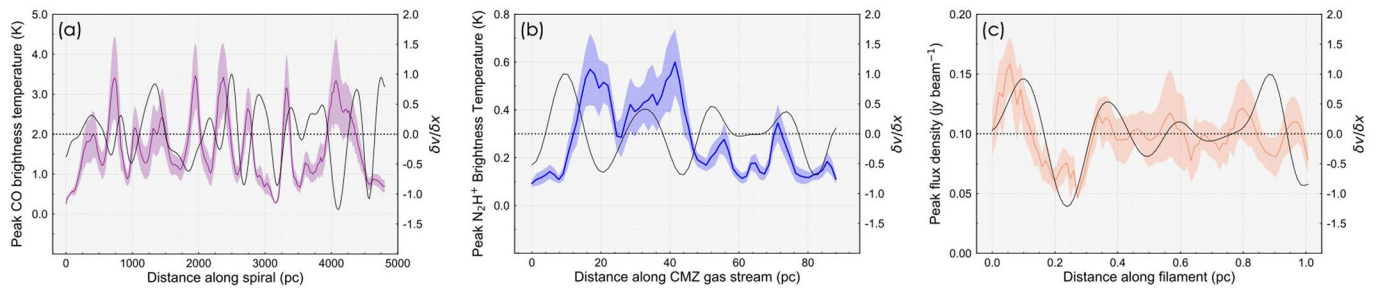
Extended Data Fig. 4 | A comparison between our density proxy and the line-of-sight velocity differential. Here we show the profile of our density proxy (coloured lines) with the normalised velocity differential (black line) along the crests of our our selected regions in NGC 4321 (**a**), the CMZ (**b**), and IRDC G035.39-00.33 (**c**), respectively. Note that in panel 'b' we show emission of N_2H^+ (1-0) rather than the column density distribution displayed in Extended Data Fig. 3c (see the discussion in the Supplementary Information). The black dotted line highlights where the derivative of the velocity is 0.0 kms^{-1} pc^{-1}.